1 **Elevated CO₂, increased leaf-level productivity and water-use efficiency during the early Miocene**

2

3 Tammo Reichgelt[1,2], William J. D'Andrea[1], Ailín del C. Valdivia-McCarthy[1], Bethany R.S. Fox[3], Jennifer

4 M. Bannister[4], John G. Conran[5], William G. Lee[6,7], Daphne E. Lee[8]

5

6 [1]Lamont-Doherty Earth Observatory, Columbia University, Palisades, New York, USA.

7 [2]Department of Geosciences, University of Connecticut, Storrs, Connecticut, USA.

8 [3]Department of Biological and Geographical Sciences, University of Huddersfield, Huddersfield, UK.

9 [4]Department of Botany, University of Otago, Dunedin, New Zealand.

10 [5]ACEBB & SGC, School of Biological Sciences, The University of Adelaide, Adelaide, Australia.

11 [6]Landcare Research, Dunedin, New Zealand.

12 [7]School of Biological Sciences, University of Auckland, Auckland, New Zealand.

13 [8]Department of Geology, University of Otago, Dunedin, New Zealand.

14 Correspondence: Tammo Reichgelt (tammo.reichgelt@uconn.edu)

15

16 **Abstract.** Rising atmospheric CO_2 is expected to increase global temperatures, plant water-use efficiency,

17 and carbon storage in the terrestrial biosphere. A CO_2 fertilization effect on terrestrial vegetation is

18 predicted to cause global greening as the potential ecospace for forests expands. However, leaf-level

19 fertilization effects, such as increased productivity and water-use efficiency, have not been documented

20 from fossil leaves in periods of heightened atmospheric CO_2. Here, we use leaf gas-exchange modeling

21 on a well-preserved fossil flora from early Miocene New Zealand, as well as two previously published

22 tropical floras from the same time period, to reconstruct atmospheric CO_2, leaf-level productivity, and

23 intrinsic water-use efficiency. Leaf gas-exchange rates reconstructed from early Miocene fossils which

24 grew at southern temperate and tropical latitudes, when global average temperatures were 5–6°C higher

25 than today reveal that atmospheric CO_2 was ~450–550 ppm. Early Miocene CO_2 was similar to projected

26 values for 2040AD, and is consistent with Earth System Sensitivity of 3–7°C to a doubling of CO_2. The

27 Southern Hemisphere temperate leaves had higher reconstructed productivity than modern analogs likely

28 due to a longer growing season. This higher productivity was presumably mirrored at northern temperate

29 latitudes as well, where a greater availability of landmass would have led to increased carbon storage in

30 forest biomass relative to today. Intrinsic water-use efficiency of both temperate and tropical forest trees

31 was high, toward the upper limit of the range for modern trees, which likely expanded the habitable range

32 in regions that could not support forests with high moisture demands under lower atmospheric CO_2.

33 Overall, early Miocene elevated atmospheric CO_2 sustained globally higher temperatures and our results

34 provide the first empirical evidence of concomitant enhanced intrinsic water-use efficiency, indicating a

35 forest fertilization effect.

36

37 **1 Introduction**

38 Terrestrial plants comprise 450 Gt of carbon, representing 80% of Earth's dry carbon (C) biomass (Bar-on

39 et al., 2018). Globally, plants draw down ~120 Gt of atmospheric C per year through photosynthesis,

40 representing the largest annual C flux on Earth (Beer et al., 2010). Total plant biomass is believed to be

41 determined in large part by atmospheric carbon dioxide concentrations (C_a), and it is predicted that future

42 increases in C_a will have a three-pronged effect on the terrestrial biosphere: 1) increased global

43 temperatures will shift the boundaries of climate zones and thereby the potential forest expanse (Rubel

44 and Kottek, 2010); 2) productivity will increase because global photosynthesis is C limited and increased

45 C_a will have a fertilization effect on the terrestrial biosphere (Zhu et al., 2016); and 3) elevated C_a will

46 increase plant water-use efficiency and reduce the threshold for physiological drought (Cernusak, 2020),

47 making more land area available for biosphere expansion (Zhou et al., 2017). Plant fossils record the

48 effect of past changes in climate, including CO_2 enrichment, and thus fossil floras provide insight into

49 changes in the carbon cycle and their effects on the terrestrial biosphere from a natural, whole-ecosystem

50 perspective.

51   The Miocene has been considered problematic for our understanding of Earth System Sensitivity

52 (ESS) to C_a, because most proxy-based C_a estimates indicate concentrations near 300 ppm (Foster et al.,

53   2017), close to pre-industrial values, yet global temperatures were 5–6 °C higher than modern (Hansen et

54   al., 2013). Enhanced radiative forcing is required to maintain such elevated early Miocene temperatures

55   (Herold et al., 2010; Hansen et al., 2013), and without elevated C_a, climate models cannot achieve such

56   high global temperatures in the Miocene (Henrot et al., 2010). The early Miocene also had an expanded

57   biosphere compared to today, including woody vegetation in locations that are currently too cold and/or

58   too dry for forests (e.g. Askin and Raine, 2000; Herold et al., 2010). A biosphere of the magnitude

59   observed in the early Miocene fossil record requires elevated temperatures and plant water-use efficiency,

60   suggesting C_a levels higher than estimated by most existing proxy reconstructions (Herold et al., 2010;

61   Henrot et al., 2010). Importantly, plant-based C_a reconstructions have challenged the consensus of low C_a

62   in the early Miocene (Kürschner and Kvaček, 2009; Reichgelt et al., 2016; Tesfamichael et al., 2017;

63   Londoño et al., 2018) and previous interpretations of alkenone-based C_a proxies are being disputed

64   (Bolton et al., 2016; Witkowski et al., 2019).

65   We applied plant gas-exchange modeling (Franks et al., 2014) to fossil leaves from the early Miocene

66   (~23 Ma) rainforest ecosystem from southern New Zealand preserved in the Foulden Maar deposit

67   (Bannister et al., 2012; Reichgelt et al., 2013; Conran et al., 2014; Lee et al., 2016) to reconstruct carbon

68   assimilation rates (A_n), intrinsic water-use efficiency (iWUE; the ratio between carbon assimilation and

69   stomatal conductance to water), and the C_a levels required to maintain these values. The same analyses

70   were performed on previously published leaf $\delta^{13}C$ and micromorphological measurements from two early

71   Miocene fossil floras from Ethiopia (Tesfamichael et al., 2017) and Panama (Londoño et al., 2018). These

72   two studies were incorporated here because they represent a similar time period (early Miocene) and the

73   authors applied the same gas-exchange methodology. Because A_n, iWUE, and C_a are interdependent

74   (Farquhar et al., 1980; Drake et al., 1997), we reconstructed these variables in concert for each fossilized

75   leaf recovered from these forest ecosystems. This allows us to make inferences concerning carbon

76   availability, productivity, and water balance in the forest.

77

78   **2 Methods**

2.1 Site Description

Foulden Maar (Fig. 1a) is a unique *Konservat-Lagerstätte* with abundantly preserved plants and insects (Kaulfuss et al., 2015; Lee et al., 2016) in southern New Zealand (45.527°S, 170.219°E). It was formed in an ancient maar-diatreme lake (Fig. 1b) at the Oligocene/Miocene boundary (Fox et al., 2015; Kaulfuss, 2017) and consists of ~100 kyr of annually laminated diatomite (Lindqvist and Lee, 2009; Fox et al., 2016). The Foulden maar-diatreme complex is part of the larger late Oligocene – late Miocene Waipiata Volcanic Field that produced a variety of maar volcanoes and scoria cones (Németh and White, 2003). Plant fossils used in this study were collected from a ~183 m long drill core (Fig. 1c). The Lauraceae-dominated rainforest (Bannister et al., 2012) surrounding the lake grew at a paleolatitude of ~50°S (Fig. 1a). The climate was marginally subtropical with a mean annual temperature of ~18°C, similar to modern day climates at 30°S (Reichgelt et al., 2019). The length of the growing season in this climate was ~10 months, compared to 5–6 months today, as reconstructed from the surface exposure macrofossil assemblage using the Climate Leaf Analysis Multivariate Program (Reichgelt et al., 2013).

2.2 Fossil leaf anatomy and paleoecology

Mummified fossil leaves were extracted from turbidite deposits that occur frequently within the Foulden Maar diatomite core (Fox et al., 2015). The diatomite is loosely consolidated allowing mummified leaves to be extracted using a combination of water and scalpels. After extraction, the leaves were cut into three pieces: one for bulk $\delta^{13}C$ analysis, one for stomatal conductance measurements, and a third as a reference specimen. Leaf $\delta^{13}C$ was measured using a Costech elemental combustion system (EA) coupled to a Delta V Plus IRMS (Thermo). In order to place measured $\delta^{13}C$ on the VPDB scale, we calibrated measurements using a two-point isotope calibration based on the USGS40 and USGS41 standards. Measurement uncertainty was calculated by replicating ~15 samples two or three times and applying averaged uncertainty to the remaining leaves. For stomatal density and geometry measurements the leaves were soaked in hydrogen peroxide (H_2O_2) with up to 40% dilution, with tetra-sodium pyrophosphate salt crystals ($Na_4P_2O_7 \cdot 10[H_2O]$), on a boiling plate at 40–50 °C for 1–2 hours (Bannister et al., 2012). When

105   the adaxial and abaxial cuticle layer could be separated, the leaf layers were cleaned of mesophyll cell

106   debris using small paintbrushes and both layers were stained with <0.5% Crystal Violet ($C_{25}N_3H_{30}Cl$) and

107   mounted on glass slides with glycerin jelly. Stomatal conductance and geometry measurements were

108   made on pictures at 100× magnification using TSView 7.1.1.2 microscope imaging software on a Nikon

109   Optiphot. Leaves were often fragmented and the cuticle wrinkled because the leaves were deposited in

110   turbidites. Moreover, there was strong divergence in overall cell and stomatal density, because we made

111   measurements on all species recovered from the sediments. To avoid systematic errors arising from

112   wrinkled cuticle, differing leaf architecture between species, or low cell counts (Retallack and Conde,

113   2020), each picture was given a standard bounding box (0.3 × 0.3 mm) on which cells were counted, to

114   calculate stomatal density. The number of cells in each bounding box ranged from 100 – 750, strongly

115   dependent on species. Five to eight pictures were taken of each leaf to constrain errors in cell density.

116   Stomatal size measurements were made using ImageJ 1.48v software (Schneider et al., 2012).

117   18 distinct leaf morphotypes were identified from the Foulden Maar drill core. Descriptions and

118   justification for identification are found in the Supplementary Information. Species identifications are

119   provided, where possible, based on paleobotanical studies from the Foulden Maar surface exposures.

120   Known species recovered from the Foulden Maar drill core are *Litsea calicarioides* (Fig. S1a),

121   *Cryptocarya taieriensis* (Fig. S1b), *C. maarensis* (Fig. S1i), *Beilschmiedia otagoensis* (Fig. S2a)

122   (Lauraceae) (Bannister et al., 2012), *Laurelia otagoensis* (Fig. S2h) (Atherospermataceae) (Conran et al.,

123   2013), and *Hedycarya pluvisilva* (Fig. S2i) (Monimiaceae) (Conran et al., 2016). Otherwise, tentative

124   genus or family identifications are provided, or unspecified morphotypic qualifiers, for leaves that could

125   not be assigned a plant group. These will henceforth be referred to as "C" (Fig. S1c), cf. Myrtaceae (Fig.

126   S1d), cf. *Ripogonum* (Fig. S1e), cf. *Myrsine* (Fig. S1f), "H" (Fig. S1g), cf. Elaeocarpaceae/Cunoniaceae

127   (Fig. S1h), cf. *Dysoxylum* (Fig. S2b), cf. *Cryptocarya* (Fig. S2c), "O" (Fig. S2d), "P" (Fig. S2e), "Q"

128   (Fig. S2f) and cf. *Endiandra* (Fig. S2g).

129   We made 375 anatomical and 80 carbon isotope measurements on 72 organically preserved fossil

130   leaves representing the 18 species collected from the Foulden Maar deposit (Fig. 1a). The affinities of

131   modern living relatives of the plant types at Foulden Maar strongly suggest that during the Miocene the

132   site was characterized by a multi-layered closed canopy rainforest ecosystem (Reichgelt et al., 2013;

133   Conran et al., 2014). In order to determine atmospheric carbon (C_a), intrinsic water-use efficiency

134   (iWUE), and carbon assimilation rates (A_n), the ecological strategies of the individual fossil species at

135   Foulden Maar need to first be established (Reichgelt and D'Andrea, 2019). Understory species rarely

136   experience light saturation and utilize respired CO_2 that has already undergone isotopic fractionation;

137   both conditions influence gas-exchange modelling results (Royer et al., 2019). Therefore, C_a

138   reconstructed from understory species cannot be considered indicative of true global C_a. Here, we

139   determine whether a fossil leaf type was likely in the canopy or the understory, based on 1) leaf $\delta^{13}C$, 2)

140   leaf cell density, and 3) sinuosity of the epidermal cell walls. A large range of leaf $\delta^{13}C$ in a single species

141   is indicative of different levels of light saturation, which indicates that this species may preferentially

142   occur in the subcanopy or in the understory (Graham et al., 2014). Leaves in the canopy, experiencing

143   light saturation, divide epidermal cells rapidly compared to leaves in the shade, leading to high cell

144   densities and relatively high leaf mass per areas in sun-exposed leaves (Šantrůček et al., 2014). Finally, a

145   high level of anticlinal cell wall sinuosity has been interpreted as indicative of low-light conditions

146   (Kürschner, 1997; Bush et al., 2017). We consider these three lines of evidence occurring in concert as

147   indicative of a canopy or subcanopy ecological preference.

148

149   **2.3 Modelling gas-exchange**

150   Atmospheric carbon dioxide (C_a), plant photosynthesis (A_n), and intrinsic water-use efficiency (iWUE)

151   are tightly linked (Farquhar et al., 1980; Drake et al., 1997), which allows us to solve for these parameters

152   iteratively, through anatomical and carbon isotope ($\delta^{13}C$) measurements of the fossil leaves. The Franks et

153   al. (2014) gas-exchange model solves for C_a, by iteratively reconstructing A_n and leaf conductance to

154   atmospheric carbon (G_c), using a Monte Carlo approach. This means that every C_a reconstruction has an

155   associated A_n and G_c value.

156

157
$$C_a = {A_n} \Big/ {G_c \times \left(1 - \frac{C_i}{C_a}\right)} \quad (1)$$

158

159 In which C_i/C_a represents the ratio of intercellular carbon to atmospheric carbon, which can be

160 reconstructed using known leaf fractionation processes: fractionation caused by diffusion (a),

161 carboxylation (b), and fractionation caused by the preferential uptake of ^{12}C to ^{13}C in photosynthesis (Δ),

162 which is also influenced by the rate at which the leaf is photosynthesizing (Farquhar et al., 1982).

163

164
$$\frac{C_i}{C_a} = \frac{\Delta - a}{b - a} \quad (2)$$

165

166 Here, a = 4.4‰ and b = 29‰ (Farquhar et al., 1982; Roeske and O'Leary, 1984). Δ can be calculated

167 from the $\delta^{13}C$ of the air, derived from Tipple et al. (2010) and measurements of leaf $\delta^{13}C$ (Farquhar and

168 Richards, 1984; Farquhar et al., 1989). Leaf and air $\delta^{13}C$ used in the Franks et al. (2014) model are

169 presented in Table S1.

170

171
$$\Delta = \frac{\delta^{13}C_{air} - \delta^{13}C_{leaf}}{1 + \delta^{13}C_{leaf}} \quad (3)$$

172

173 G_c is determined by the maximum capacity for conductance of a leaf surface (G_{max}), the ratio of

174 operational conductance to G_{max} (ζ), boundary layer conductance (G_b), and mesophyll conductance (G_m)

175 (Franks et al., 2014).

176

177
$$G_c = \left(\frac{1}{G_b} + \frac{1}{\zeta \times G_{max}} + \frac{1}{G_m}\right)^{-1} \quad (4)$$

178

179   G_b, ζ, and G_m are all changeable under natural conditions (e.g. Schuepp, 1993; Niinemets et al., 2009;

180   Londoño et al., 2018) and it is highly disputed if these variables can be determined from fossil leaf

181   material at all (e.g. McElwain et a., 2016; Soh et al., 2017). However, we adopt a standardized approach

182   put forward by Franks et al. (2014) to obtain input for these variables. $G_b = 2 \pm 0.1$ mol m^{-2} s^{-1}, $\zeta = 0.2 \pm$

183   0.02 (Franks et al., 2009; Dow et al., 2014), and G_m is determined using an empirical calibration (Evans

184   and Von Caemmerer, 1996).

185

186    $$G_m = 0.013 \times A_n \quad (5)$$

187

188   G_{max} is determined using predominantly measurable anatomical features of the fossil leaf cuticle (Franks

189   and Beerling, 2009): stomatal density (SD), maximum aperture surface area (a_{max}), pore depth (p_d), and

190   the ratio of diffusivity of CO_2 in air over the molar volume of air (d/v), here taken as 0.000714 mol m^{-1} s^{-1}

191   (Marrero and Mason, 1972).

192

193    $$G_{max} = {d}/{v} \times SD \times \frac{a_{max}}{p_d + \frac{\pi}{2}\sqrt{a_{max}/\pi}} \quad (6)$$

194

195   In this equation, SD can be measured directly from the leaf, p_d is assumed to be the same as guard cell

196   width (gcw), and a_{max} is determined assuming a circular opening for the aperture, with the measurable

197   pore length (p_l) as the diameter (Franks et al., 2014).

198

199    $$a_{max} = \pi \times \frac{p_l}{4} \quad (7)$$

200

201   Measurements of SD, gcw and p_l used in the Franks et al. (2014) gas-exchange model are presented in

202   Table S1.

203

204   Because A_n is required to solve G_m, G_c is solved iteratively, though G_c is largely determined by

205   measurable anatomical parameters. However, A_n is also solved iteratively, as it is dependent on C_a and the

206   carbon saturation value (Γ), set at 40 ppm (Franks et al., 2013).

207

208
$$A_n \approx A_0 \times \frac{(C_a - \Gamma) \times (C_{a0} + 2\Gamma)}{(C_a + 2\Gamma) \times (C_{a0} - \Gamma)} \quad (8)$$

209

210   In which A_0 is the photosynthetic rate of a modern model species that can represent the fossil species'

211   photosynthetic rate, and C_{a0} is the atmospheric carbon dioxide level at which A_0 was measured. A_0 for

212   each fossil species was derived from the compilation of photosynthetic rates presented in Reichgelt and

213   D'Andrea (2019). For fossil leaves with known modern relatives, we constrained the possible A_0 range by

214   only including modern relatives within the same family or order, i.e. Lauraceae for *Litsea calicarioides*,

215   *Cryptocarya taieriensis*, *C. maarensis*, cf. *Cryptocarya*, *Beilschmiedia otagoensis* and cf. *Endiandra*,

216   Myrtaceae for cf. Myrtaceae, Liliales for cf. *Ripogonum*, Primulaceae for cf. *Myrsine*, Elaeocarpaceae and

217   Cunoniaceae for cf. Elaeocarpaceae/Cunoniaceae, Meliaceae for cf. Meliaceae, Atherospermataceae for

218   *Laurelia otagoensis,* and Laurales for *Hedycarya pluvisilva*. Then, following the method of constraining

219   A_0 of modern living relatives presented in Reichgelt and D'Andrea (2019), only A_0 values of plants with

220   similar growth forms to the fossil plants, and growing in similar light environments as Foulden Maar were

221   included. A_0 and C_{a0} used in the Franks et al. (2014) model, and associated ecology of fossil leaf types is

222   shown in Table S2.

223

224   The Franks et al. (2014) gas-exchange model thus iteratively solves for C_a, A_n, and G_c. However, only

225   leaves derived from canopy trees are likely to represent these values at light saturation. Moreover, plants

226   in the understory assimilate a mix of atmospheric and respired CO_2, which has already undergone

227   fractionation processes, making the calculated C_i/C_a problematic. Therefore, we present the results for C_a,

228   A_n, and G_c of leaf types most likely to be derived from canopy trees separately, as they are more likely to

229   not have a systematic skew.

230   iWUE is defined as the ratio between A_n and stomatal conductance to water (Feng, 1999).

231

232

$$iWUE = \frac{A_n}{G_w} \quad (9)$$

233

234   Due to the different rates at which carbon dioxide and water vapor diffuse in air, a transformation of G_c is

235   required to calculate G_w.

236

237

$$G_w = 1.6 \times G_c \quad (10)$$

238

239   Finally, cumulative annual carbon uptake through photosynthesis (A_{tot}) can be calculated in gC m^{-2} yr^{-1},

240   by transferring from moles to grams, including a measure for the relative time the leaf is assimilating

241   carbon (ζ), and the length of the growing season.

242

243

$$A_{tot} = (2.6 \times \zeta \times A_n \times t_g) \times 12 \quad (11)$$

244

245   In which t_g is the length of the growing season in months, which we can derive from the fossil plant

246   assemblage (Reichgelt et al., 2019), using the method of Spicer et al. (2009). G_w, A_{tot}, and iWUE values

247   for *Litsea calicarioides*, *Cryptocarya taieriensis*, *C. maarensis*, cf. Elaeocarpaceae/Cunoniaceae, and cf.

248   Myrtaceae are presented in Table S3. The modern reference A_n and G_w data are derived from Maire et al.

249   (2015), which, using transform functions 9 and 11, we also used to calculate iWUE and A_{tot}.

250

251   **2.4 Comparison to Earth System Sensitivity**

252   Earth System Sensitivity to C_a (ESS) is the amount of temperature increase expected under a doubling of

253   atmospheric CO_2. This sensitivity is likely not static in Earth's history and is dependent on, among other

254   aspects, continental configuration and ocean circulation patterns (Royer, 2016). Here, we estimate global

255   surface temperature for the early Miocene following the approach of Hansen et al. (2013). We then use

256   these temperature estimates along with a broad range of commonly cited Neogene ESS, of 3–7°C

257   (Hansen et al., 2013; Royer, 2016), to provide a model for the expected early Miocene C_a. Following this

258   model, ultimately means that a doubling of C_a compared to pre-industrial levels is expected when an

259   increase of global average surface temperatures (T_s) of 3–7°C compared to modern occurs.

260   Compiled deep-sea benthic foraminifera $\delta^{18}O$ data of the last 30 million years (Zachos et al., 2001)

261   were averaged into 20 kyr time bins. Deep-sea temperatures (T_d) were then calculated using the linear

262   transfer functions of Hansen et al. (2013), which depend on the presence of sea-ice.

263

264
$$T_d = 5 - 8 \times \frac{\delta^{18}O - 1.75}{3} \; IF \; (\delta^{18}O < 3.25) (12)$$

265
$$T_d = 1 - 4.4 \times \frac{\delta^{18}O - 3.25}{3} \; IF \; (\delta^{18}O > 3.25) (13)$$

266

267   T_s was then calculated for post-Pliocene using:

268

269
$$T_s = 2 \times T_d + 12.25 \;\; (14)$$

270   For the Pliocene:

271
$$T_s = 2.5 \times T_d + 12.15 \;\; (15)$$

272

273   And for pre-Pliocene we assumed that T_s changed linearly with T_d, by a factor of 1.5.

274

275
$$\Delta T_s = 1.5 \times \Delta T_d \;\; (16)$$

276

277 C_a based on an ESS range of 3–7°C was then calculated using the resulting T_s.

278

$$C_a = 310 \times \frac{T_{s[x]} - T_{s[0]}}{2 \times ESS} + 310 \ (17)$$

280

281 In which $T_{s[x]}$ is the calculated average global surface temperature at time x, $T_{s[0]}$ is the modern day

282 average global surface temperature, and 310 represents pre-industrial C_a.

283

3 Results and Discussion

3.1 Southern Temperate Rainforest Paleoecology

286 Modern day Lauraceae rainforests in New Zealand have a single dominant canopy tree, *Beilschmiedia*

287 *tawa*, and its farthest southern extent is ~42°S (Leathwick, 2001), which is the farthest southern

288 occurrence of any arborescent Lauraceae species in the world. Rainforests further south in New Zealand

289 are usually dominated by Nothofagaceae or Podocarpaceae, and the only modern-day forests at ~50°S are

290 the Magellanic Subpolar Forests in southern South America. Low-growing Podocarpaceae/Nothofagaceae

291 forests, similar to modern forests in southern New Zealand and southern South America, dominated

292 Antarctic vegetation during the early Miocene (Askin and Raine, 2000) and the Foulden Maar rainforest

293 included at least ten Lauraceae species (Bannister et al., 2012), emphasizing the expanded biosphere

294 potential in the early Miocene compared to today (Herold et al., 2010).

295   We identify *Litsea calicarioides*, *Cryptocarya maarensis*, *C. taieriensis*, cf.

296 Elaeocarpaceae/Cunoniaceae, and cf. Myrtaceae as the most probable canopy components because they

297 lack characteristics typical of understory components, 1) the large range of leaf δ^{13}C values and relatively

298 low overall leaf δ^{13}C values (Graham et al., 2014), 2) low cell densities (Kürschner, 1997; Bush et al.,

299 2017) (Fig. 2 a,b), and 3) the undulating or sinuous cell walls (Kürschner, 1997; Bush et al., 2017).

300 Modern day *Litsea calicaris* in New Zealand is also part of the canopy, though rarely dominant (de

301 Lange, 2020), whereas *Cryptocarya* is extinct in New Zealand. Members of Elaeocarpaceae, Cunoniaceae

302 and Myrtaceae in modern day New Zealand, such as *Weinmannia racemosa* (Cunoniaceae) and

303 *Metrosideros robusta* (Myrtaceae) can attain heights of over 25 meters (de Lange, 2020).

304   The most likely subcanopy or understory taxa were cf. *Ripogonum*, cf. *Myrsine*, "O", and cf.

305 *Dysoxylum*, because leaf fossils of these types have low overall leaf $\delta^{13}C$, relatively low cell densities, and

306 sinuous or undulating cells (Fig. S1e,f, S2b,d). *Ripogonum scandens* in modern day New Zealand is a

307 twining forest liana, often found in the understory, *Myrsine* comprises several species of shrubs and small

308 trees; whereas *Dysoxylum spectabile* in modern day New Zealand is a medium-sized tree (de Lange,

309 2020). The affinity of morphotype "O" is unclear, but likely represents a now extinct plant group in New

310 Zealand. *Hedycarya. pluvisilva*, *Laurelia. otagoensis*, cf. *Cryptocarya*, cf. *Endiandra*, *Beilschmiedia.*

311 *otagoensis*, "C", "H", "P", and "Q", all displayed some variation in features that are typical of understory

312 or canopy components and occurred in relatively low abundance, and are therefore considered of

313 uncertain ecological affinity.

314

315 **3.2 Earliest Miocene CO$_2$**

316   Gas-exchange modeling (Franks et al., 2014) of canopy leaves throughout the Foulden Maar core

317 indicates that C_a (±1σ) was 445 +618 / -100 ppm, whereas reconstructed C_a from understory elements

318 yields C_a of 622 +3017 / -161 ppm (Fig. 2c), consistent with understory plants assimilating respired CO_2

319 that has undergone prior fractionation processes, as well as experiencing elevated levels of C_a under the

320 canopy (Graham et al., 2014; Royer et al., 2017). Prior work on the Foulden Maar core established three

321 different phases based on bulk organic $\delta^{13}C$ (Fig. 1c), fatty acid $\delta^{13}C$, and fatty acid δD: Phase I (80–105

322 m depth) with high $\delta^{13}C$ and low δD, Phase II (55–65 m depth) with low $\delta^{13}C$ and high δD, and Phase III

323 (0–45 m depth) with high $\delta^{13}C$ and low δD (Reichgelt et al., 2016). Phase III can be further subdivided

324 into Phase IIIa (30–45 m depth) and IIIb (0–20 m depth), as Phase IIIa exhibits a period of low fatty acid

325 $\delta^{13}C$ and high δD, which is not expressed in bulk organic $\delta^{13}C$ (Reichgelt et al., 2016). Gas-exchange

326 modelling on leaves from these phases (Fig. 1c) suggest that during Phase II and IIIa C_a may have been

327   elevated (C_a = 529 +1159 / -125 and C_a = 538 +769 / -181 ppm, respectively) compared to Phase I and

328   Phase IIIb (C_a = 444 +572 / -95 and 442 +1219 / -110 ppm, respectively) (Fig. 3). Although gas-exchange

329   modeling input reconstructed differing C_a between phases, differences in overall conductance parameters,

330   such as stomatal density and leaf $\delta^{13}C$, are not apparent (Table S1), despite differences in bulk $\delta^{13}C$, fatty

331   acid $\delta^{13}C$, and δD (Reichgelt et al., 2016). This is likely the result of non-uniform species responses to

332   environmental changes in a complex multi-layered rainforest ecosystem, such as at Foulden Maar.

333   The advantage of using gas-exchange modeling to reconstruct C_a from multiple species is that the

334   uncertainty is quantified and constrained, greatly reducing the potential for systematic error in the final

335   estimate (Reichgelt and D'Andrea, 2019; Royer et al., 2019). Along with the enhanced accuracy comes a

336   more comprehensive appraisal of uncertainty than is achieved using other proxy approaches (Fig. 4).

337   Proxy error propagation is based on mechanistic variability, grounded in known physical and

338   physiological limits of plant gas-exchange that are understood to be universal (Franks et al., 2014). This

339   differs from empirical proxies, whose uncertainty representation is based on calibration error of modern-

340   day observations without mechanistic constraints. Our canopy C_a estimate (445 +618 / -100 ppm, Fig. 2c)

341   is independent of calibration error, based on universal gas-exchange mechanisms, and represents plant

342   vegetative organs of multiple plant species that directly interacted with the available pool of atmospheric

343   carbon dioxide. Previous C_a estimates from the Oligocene/Miocene boundary based on boron isotopes

344   and paleosol carbonates are generally lower than our estimates (Ji et al., 2018; Greenop et al., 2019) (Fig.

345   4b), whereas C_a estimates based on stomatal index and recent alkenone-based C_a estimates are more

346   similar to our results (Kürschner et al., 2008; Super et al., 2018).

347   Reconstructions of globally elevated temperatures of 5–6 °C in the early Miocene (Hansen et al.,

348   2013) with a C_a of ~300 ppm (Ji et al., 2018; Greenop et al., 2019) upsets the expected ESS to C_a during

349   this period (Henrot et al., 2010). Geochemical C_a proxy estimates consistently produce C_a estimates that

350   are too low to satisfy ESS to C_a prior to the Pliocene (Royer, 2016) (Fig. 4a,b). Estimates from the fossil

351   leaf-based stomatal index proxy for C_a (Kürschner et al., 2008) on the other hand do indicate a positive

352   correlation between temperature and C_a in the Neogene (Fig. 4a). At present, there are too few studies that

353 reconstruct C_a using gas-exchange modeling to allow for a full comparison to other C_a proxies; however,

354 our C_a estimates of ~450–550 ppm are in line with the ESS to C_a in the early Miocene (Fig. 4a,b), based

355 on modelling experiments (Herold et al., 2010; Henrot et al., 2010). Moreover, thus far, Neogene C_a

356 estimates reconstructed using gas-exchange methods (Reichgelt et al., 2016; Tesfamichael et al., 2017;

357 Londoño et al., 2018; Moraweck et al., 2019) appear to agree with the suggested ESS to C_a (Fig. 4a,b).

358 Bulk organic and leaf wax $\delta^{13}C$ values reveal a ~4‰ decrease at Foulden Maar over a 10-meter

359 interval at the beginning of Phase II (55–65 m depth), likely representing a time period of <10 kyr (Fox et

360 al., 2016). This shift in isotopic composition suggests a substantial change in the global carbon cycle

361 (Reichgelt et al., 2016). The mode of reconstructed values in this study suggests and increase of ~450 to

362 550 from Phase I to Phase II (Fig. 3). The C_a values stay near 550 ppm throughout Phase II and Phase

363 IIIa, representing a 20–40 kyr time period (Fig. 3). Absolute dating of Foulden Maar based on

364 paleomagnetic reversals in the core, annual lamination of lake sediments, and basalt-derived Ar/Ar dates

365 indicates that the deposition of the Foulden Maar sediment coincided with the termination of the earliest

366 Miocene (Mi-1) glaciation of Antarctica (Fox et al., 2015). Interestingly, an increase in C_a from ~450 to

367 ~550 ppm at the termination of Mi-1 is consistent with modeling studies indicating that $C_a > 500$ ppm is

368 necessary to terminate a large-scale Antarctic glaciation (DeConto et al., 2008). We note that with the

369 current data available, it is not possible to exclude the possibility that modeled C_a changes in the record

370 were influenced by canopy density changes or regional hydroclimate. However, our observations from

371 Foulden Maar are inconsistent with hydrological, ecological or C_a changes as the sole driver of plant

372 physiological response (Reichgelt et al., 2016), and it is more likely that two or more of these parameters

373 changed in concert.

374

375 **3.3 Elevated CO₂ and the early Miocene biosphere**

376 The Foulden Maar Miocene rainforest was primarily evergreen (Lee et al., 2016). The main Miocene

377 canopy trees at Foulden Maar, *Litsea calicarioides*, *Cryptocarya taieriensis*, *C. maarensis*, cf.

378 Elaeocarpaceae/Cunoniaceae and cf. Myrtaceae, had relatively high iWUE (Miocene iWUE first quartile

379   [Q_1] – third quartile [Q_3] = 70–101) compared to modern evergreen trees (evergreen iWUE Q_1–Q_3 = 31–

380   73) (Fig. 5a). Reconstructed iWUE from tropical early Miocene plants (Tesfamichael et al., 2017;

381   Londoño et al., 2018) is slightly higher (Q_1–Q_3 = 80–125) (Fig. 5a). The difference between reconstructed

382   Miocene iWUE and that of modern deciduous trees is greater still (deciduous iWUE Q_1–Q_3 = 27–52),

383   consistent with the expectation that increased C_a favors evergreen trees (Niinemets et al., 2011; Soh et al.,

384   2019). In the method of reconstruction used here, iWUE is ultimately an expression of leaf $\delta^{13}C$ and

385   conductance (see Methods section 2.3). Therefore, similar to reconstructed C_a iWUE may be sensitive to

386   environmental factors other than C_a. For example, leaf $\delta^{13}C$ can change in response to edaphic conditions

387   and precipitation (e.g. Kohn, 2016; Cornwell et al., 2018), as well as vapor pressure deficit (VPD) (Franks

388   et al., 2013). The climate of Foulden Maar in the early Miocene was warm-temperate to subtropical,

389   compared to the cool-temperate forests in southern New Zealand today (Reichgelt et al., 2019). Though

390   reconstructed relative humidity at Foulden Maar is within the range of modern New Zealand forest

391   biomes, the average monthly VPD was 500–700 Pa, compared to 250–450 Pa today (Fig. S3), which may

392   result in a similar reconstructed iWUE as under elevated C_a (Franks et al., 2013). However, the

393   reconstructed ecosystem at Foulden Maar is a broad-leaved humid rainforest (Bannister et al., 2012),

394   which likely had a high annual moisture surplus (Reichgelt et al., 2019). Increased water-use efficiency in

395   response to relatively high VPD compared to modern would only be a positive trade-off if water

396   availability were limiting. Additionally, reconstructed iWUE from both temperate and tropical early

397   Miocene floras are high compared to modern, suggesting a global signal, such as would be expected to

398   globally elevated C_a; not from VPD as the early Miocene tropics would not be warmer than today (Herold

399   et al., 2010). Most importantly, the modern iWUE data (Fig. 5a) are from a global database that includes

400   environments with annual moisture deficits (Maire et al., 2015). Because reconstructed early Miocene

401   iWUE is higher even than modern plants experiencing high VPD, we argue that VPD differences cannot

402   explain the high iWUE values of the early Miocene, and that increased efficiency due to higher C_a is the

403   best explanation.

404   In contrast to iWUE, reconstructed conductance to water (G_w) for Miocene trees is similar to the

405   modern-day range at the same latitude (Fig. 5b), a somewhat surprising result because G_w is expected to

406   be reduced in high C_a climates (Franks and Beerling, 2009). Studies on modern forests also suggest the

407   absence of a reduction in G_w to enhanced C_a (Yang et al., 2016; Gimeno et al., 2018), or even an increase

408   in the G_w (Frank et al., 2015). A longer growing season together with increasing VPD was proposed to

409   explain increasing G_w in modern European forests (Frank et al., 2015). Similarly, a relatively high water

410   flux from the forest to the atmosphere due to high water supply (Reichgelt et al., 2019) and high VPD

411   (Fig. S3) could explain the broad similarity in the range of modern and early Miocene G_w, despite higher

412   C_a. The early Miocene G_w from tropical latitudes are within the range of modern evergreen tropical trees,

413   though relatively low (Early Miocene Q1–Q3: 0.08–0.13 mol m^{-2} s^{-1}, modern evergreen Q1–Q3: 0.07–0.2

414   mol m^{-2} s^{-1}) (Fig. 5b).

415   A longer growing season likely resulted in the high total annual carbon flux (A_{tot}) to the biosphere

416   reconstructed for Foulden Maar (Fig. 5c). Early Miocene trees at 50°S likely assimilated A_{tot} Q$_1$–Q$_3$ =

417   265–696 gC m^{-2} yr^{-1}, in comparison to A_{tot} Q$_1$–Q$_3$ = 108–182 gC m^{-2} yr^{-1} in modern evergreen forests, and

418   A_{tot} Q$_1$–Q$_3$ = 249–410 gC m^{-2} yr^{-1} in modern deciduous forests at the same latitude (Fig. 5c). Early

419   Miocene tropical trees appear to have slightly higher total annual carbon flux (A_{tot} Q$_1$–Q$_3$ = 596–1220 gC

420   m^{-2} yr^{-1}) than today (A_{tot} Q$_1$–Q$_3$ = 329–721 gC m^{-2} yr^{-1}), which, with a year-round growing season in the

421   early Miocene (like today), is likely attributable to a leaf-level fertilization effect, similar to what is

422   observed in modern carbon fertilization experiments (Norby et al., 2003; Bader et al., 2013; Yang et al.,

423   2016). Although this estimate cannot take the number of leaves per unit area into account, these results

424   suggest enhanced leaf-level productivity during higher than modern C_a in the early Miocene.

425   The methods used in this study provide an alternate approach to controlled carbon fertilization

426   experiments, such as the Free Air Carbon Enrichment (FACE) experiments (e.g. Long et al., 2004),

427   toward investigating the effect of increased C_a on the biosphere. FACE experiments provide data on the

428   physiological effects of carbon enrichment on species that evolved under, or had thousands of years to

429   adapt to pre-industrial C_a ($\approx$ 280 ppm), and the physiological changes detected in canopy species are

430   measured as a direct response or over leaf generations (e.g. Norby et al., 2003; Yang et al., 2016). By

431   contrast, our data provide an insight into species that evolved under higher than pre-industrial C_a and had

432   many generations of individuals to adapt to incrementally slow changes. The direct, or multi-year

433   physiological response of modern forest trees to enhanced C_a is non-linear and non-uniform (e.g. Long et

434   al., 2004; Ainsworth and Long, 2005), and therefore further investigations into the physiology of ancient

435   plants operating in high-CO_2 worlds are needed to reveal the complexity of plant responses over

436   evolutionary timescales.

437

438   **4 Conclusions**

439   Leaf-level gas-exchange derived C_a estimates suggest that early Miocene atmospheric CO_2 was higher

440   than pre-industrial levels at 450–550 ppm, further solidifying the growing consensus of relatively high

441   early Miocene global temperatures maintained by high atmospheric CO_2 (Kürschner et al., 2009;

442   Tesfamichael et al., 2017; Super et al., 2018; Londoño et al., 2018; Moraweck et al., 2019). A relatively

443   high C_a in the early Miocene also satisfies an Earth System Sensitivity of 3–7°C (Hansen et al., 2013;

444   Royer, 2016). A potential shift in atmospheric CO_2 from 450 to 550, and back to 450, is recorded in the

445   100 kyr of sedimentation and leaf deposition at Foulden Maar. A disruption of the regional carbon and

446   hydrological cycle was also recorded in leaf-wax $\delta^{13}C$ and δD (Reichgelt et al., 2016), and may be linked

447   to the Antarctic deglaciation at the termination of the Mi-1 (DeConto et al., 2008; Fox et al., 2015;

448   Liebrand et al., 2017).

449   The first record is provided of increased Miocene leaf-level intrinsic water-use efficiency in both

450   temperate New Zealand and the tropics, and we provide evidence for increased leaf-level productivity in

451   temperate New Zealand. Enhanced productivity and water-use efficiency on other landmasses in

452   temperate latitudes during the early Miocene, such as North America, Australia, and Asia, would have

453   had a major impact on the global carbon and water cycles. Our gas-exchange results from New Zealand,

454   supplemented with results from Ethiopia (Tesfamichael et al., 2017) and Panama (Londoño et al., 2018)

455   provide empirical evidence for high water-use efficiency in the globally warmer world of the early

456   Miocene, associated with elevated C_a. Tropical trees with high water-use efficiency compared to modern,

457   would have likely facilitated forest survival in climates where currently tropical savannas and grasslands

458   exist. These high water-use efficiency forests in the tropics likely persisted until the late Miocene when

459   reduced C_a (Mejía et al., 2017) started favoring the expansion of grasslands, in particular grasslands with

460   the C_4 pathway that is more efficient under low C_a and high temperatures (Strömberg, 2011; Polissar et

461   al., 2016).

462   Emission scenarios suggest that atmospheric CO_2 will reach our reconstructed early Miocene values of

463   450 ppm by 2030–2040 CE. While the global temperature response may lag the C_a increase, and forest

464   habitat expansion is hampered by the slow dispersal and growth rate of climax forest trees and

465   anthropogenic influence (e.g., forest fragmentation and fire), early Miocene water-use efficiency and

466   productivity estimates provide insight into future-biosphere potential, as well as into selective pressures

467   that influence the types of plants that may proliferate under future elevated C_a.

468

476

477   **Author contributions.** TR and WJD conceived of the idea and performed data analyses. BRSF and DEL

478   collected sediment core, BRSF and TR sampled the sediment core, JGC and JMB identified fossil leaf

479   taxa. ACVM and TR gathered data from fossil leaves. TR and WJD wrote the paper and all authors

480   contributed to the final manuscript.

481

482 **Competing interests.** The authors declare no competing interests.

483

484 **References**

485 Ainsworth, E. A. and Long, S. P.: What have we learned from 15 years of free-air CO_2 enrichment
486   (FACE)? A meta-analytic review of the responses of photosynthesis, canopy properties and plant
487   production to rising CO_2, New Phytologist, 165, 351–372, 2005.

488 Askin, R. A. and Raine, J. I.: Oligocene and early Miocene terrestrial palynology of the Cape Roberts
489   drillhole CRP-2/2A, Victoria Land Basin, Antarctica, Terra Antartica, 7, 493–501, 2000.

490 Bader, M. K.-F., Leuzinger, S., Keel, S. G., Siegwolf, R. T. W., Hagedorn, F., Schleppi, P. and Körner,
491   C.: Central European hardwood trees in a high CO_2 future: synthesis of an 8-year forest canopy CO_2
492   enrichment project, Journal of Ecology, 101, 1509–1519, 2013.

493 Bannister, J. M., Conran, J. G., and Lee, D. E.: Lauraceae from rainforest surrounding an early Miocene
494   maar lake, Otago, southern New Zealand, Review of Palaeobotany and Palynology, 178, 13–34, 2012.

495 Bar-On, Y. M., Philips, R., and Milo, R.: The biomass distribution on Earth, PNAS, 115, 6506–6511,
496   2018.

497 Beer, C., Reichstein, M., Tomelleri, E., Ciais, P., Jung, M., Carvalhais, N., Rödenbeck, C., Arain, M. A.,
498   Baldocchi, D., Bonan, G. B., Bondeau, A., Cescatti, A., Lasslop, G., Lindroth, A., Lomas, M.,
499   Luyssaert, S., Margolis, H., Oleson, K. W., Roupsard, O., Veenendaal, E., Viovy, N., Williams, C. J.,
500   Woodward, F. I., and Papale, D.: Terrestrial gross ccarbon dioxide uptake: Global distribution and
501   covariation with climate, Science, 329, 834–838, 2010.

502 Bolton, C. T., Hernández-Sánchez, M. T., Fuertes, M.-Á., González-Lemos, S., Abrevaya, L., Mendez-
503   Vicente, A., Flores, J.-A., Probert, I., Giosan, L., Johnson, J., and Stoll, H. M.: Decrease in
504   coccolithophore calcification and CO_2 since the middle Miocene, Nature Communications, 7, 1–13,
505   2016.

506 Boyden, J. A., Müller, R. D., Gurnis, M., Torsvik, T. H., Clark, J. A., Turner, M., Ivey-Law, H., Watson,
507   R. J., and Cannon, J. S.: Next-generation plate-tectonic reconstructions using GPlates. In:
508   Geoinformatics: Cyberinfrastructures for the Solid Earth Sciences, Keller, G. R. and Baru, C. (Eds.),
509   Cambridge University Press, 2011.

510 Bush, R. T., Wallace, J., Currano, E. D., Jacobs, B. F., McInerney, F. A., Dunn, R. E., and Tabor, N. J.:
511   Cell anatomy and leaf $\delta^{13}C$ as proxies for shading and canopy structure in a Miocene forest from
512   Ethiopia, Palaeogeography, Palaeoclimatology, Palaeoecology, 485, 593–604, 2017.

513 Cernusak, L. A.: Gas exchange and water-use efficiency in plant canopies, Plant Biology, 22, 52–67,
514   2020.

515 Conran, J. G., Bannister, J. M., and Lee, D. E.: Fruits and leaves with cuticle of *Laurelia otagoensis* sp.
516   nov. (Atherospermataceae) from the early Miocene of Otago (New Zealand), Alcheringa, 37, 1–14,
517   2013.

518 Conran, J. G., Lee, W. G., Lee, D. E., Bannister, J. M., and Kaulfuss, U.: Reproductive niche
519   conservatism in the isolated New Zealand flora over 23 million years, Biology Letters, 10, 20140647,
520   2014.

521 Conran, J. G., Bannister, J. M., Mildenhall, D. C., and Lee, D. E.: *Hedycarya* macrofossils and associated
522   *Planarpollenites* pollen from the early Miocene of New Zealand, American Journal of Botany, 103,
523   938–956, 2016.

524 Cornwell, W. K., Wright, I. J., Turner, J., Maire, V., Barbour, M. M., Cernusak, L. A., Dawson, T.,
525   Ellsworth, D., Farquhar, G. D., Griffiths, H., Keitel, C., Knohl, A., Reich, P. B., Williams, D. G.,
526   Bhaskar, R., Cornelissen, J. H. C., Richards, A., Schmidt, S., Valladares, F., Körner, C., Schulze, E.-
527   D., Buchmann, N., and Santiago, L. S.: Climate and oils together regulate photosynthetic carbon
528   isotope discrimination within C_3 plants worldwide, Global Ecology and Biogeography, 27, 1056–
529   1067, 2018.
530 DeConto, R. M., Pollard, D., Wilson, P. A., Pälike, H., Lear, C. H., and Pagani, M.: Thresholds for
531   Cenozoic bipolar glaciation, Nature, 455, 652–656, 2008.
532 De Lange, P. J.: Fact Sheet (content continuously updated). New Zealand Plant Conservation Network.
533   https://www.nzpcn.org.nz (27 May, 2020).
534 Dow, G. J., Bergmann, D. C., and Berry, J. A.: An integrated model of stomatal development and leaf
535   physiology, New Phytologist, 201, 1218–1226, 2014.
536 Drake, B. G., Gonzàlez-Meler, M. A., and Long, S. P.: More efficient plants: A consequence of rising
537   atmospheric CO_2?, Annual Review of Plant Physiology and Plant Molecular Biology, 48, 606–639,
538   1997.
539 Evans, J. R. and Von Caemmerer, S.: Carbon dioxide diffusion inside leaves, Plant Physiology, 110, 339–
540   346, 1996.
541 Farquhar, G. D., von Caemmerer, S., and Berry, J. A.: A biochemical model of photosynthetic CO_2
542   assimilation in leaves of C_3 species, Planta, 149, 78–90, 1980.
543 Farquhar, G. D., O'Leary, M. H., and Berry, J. A.: On the relationship between carbon isotope
544   discrimination and the intercellular carbon dioxide concentration in leaves, Australian Journal of Plant
545   Physiology, 9, 121–137, 1982.
546 Farquhar, G. D. and Richards, R. A.: Isotopic composition of plant carbon correlates with water-use
547   efficiency of wheat genotypes, Australian Journal of Plant Physiology, 11, 539–552, 1984.
548 Farquhar, G. D., Ehleringer, J. R., and Hubick, K. T.: Carbon isotope discrimination and photosynthesis,
549   Annual Review of Plant Physiology and Plant Molecular Biology, 40, 503–537, 1989.
550 Foster, G. L., Royer, D. L., and Lunt, D. J.: Future climate focing potentially without precedent in the last
551   420 million years, Nature Communications, 8, 14845, 2017.
552 Feng, X.: Trends in intrinsic water-use efficiency of natural trees for the past 100–200 years: a response
553   to atmospheric CO_2 concentration, Geochimica et Cosmochimica Acta, 63, 1891–1903, 1999.
554 Fox, B. R. S., Wartho, J.-A., Wilson, G. S., Lee, D. E., Nelson, F. E., and Kaulfuss, U.: Long-term
555   evolution of an Oligocene/Miocene maar lake from Otago, New Zealand, Geochemistry, Geophysics,
556   Geosystems, 16, 59–76, 2015.
557 Fox, B. R. S., Wilson, G. S., and Lee, D. E.: A unique annually laminated maar lake sediment record
558   shows orbital control of Southern Hemisphere midlatitude climate across the Oligocene-Miocene
559   boundary, Geological Society of America Bulletin, 128, 609–626, 2016.
560 Frank, D. C., Poulter, B., Saurer, M., Esper, J., Huntingford, C., Helle, G., Treydte, K., Zimmermann, N.
561   E., Schleser, G. H., Ahlström, A., Ciais, P., Friedlingstein, P., Levis, S., Lomas, M., Sitch, S., Viovy,
562   N., Andreu-Hayles, L., Bednarz, Z., Berninger, F., Boettger, T., D'Alessandro, H., Kalela-Brundin, M.,
563   Krapiec, M., Leuenberger, M., Loader, N. J., Marah, H., Masson-Delmotte, V., Pazdur, A., Pawelczyk,
564   S., Pierre, M., Planells, O., Pukiene, R., Reynolds-Henne, C. E., Rinne, K. T., Saracino, A., Sonninen,
565   E., Stievenard, M., Switsur, V. R., Szczepanek, E., Szychowska-Krapiec, L., Todaro, L., Waterhouse,
566   J. S., and Weigl, M.: Water-use efficiency and transpiration across European forests during the
567   Anthropocene, Nature Climate Change, 5, 579–583, 2015.

Franks, P. J. and Beerling, D. J.: Maximum leaf conductance driven by CO_2 effects on stomatal size and density over geologic time, PNAS, 106, 10343–10347, 2009.

Franks, P. J., Drake, P. L., and Beerling, D. J.: Plasticity in maximum stomatal conductance constrained by negative correlation between stomatal size and density: an analysis using *Eucalyptus globulus*, Plant, Cell and Environment, 32, 1737–1748, 2009.

Franks, P. J., Adams, M. A., Amthor, J. S., Barbour, M. M., Berry, J. A., Ellsworth, D. S., Farquhar, G. D., Ghannoum, O., Lloyd, J., McDowell, N. G., Norby, R. J., Tissue, D. T., and von Caemmerer, S.: Sensitivity of plants to changing atmospheric CO_2 concentration: from the geological past to the next century, New Phytologist, 197, 1077–1094, 2013.

Franks, P. J., Royer, D. L., Beerling, D. J., van de Water, P. K., Cantrill, D. J., Barbour, M. M., and Berry, J. A.: New constraints on atmospheric CO_2 concentration for the Phanerozoic, Geophysical Research Letters, 41, 4685–4694, 2014.

Gimeno, T. E., McVicar, T. R., O'Grady, A. P., Tissue, D. T. and Ellsworth, D. S.: Elevated CO_2 did not affect the hydrological balance of a mature native *Eucalyptus* woodland, Global Change Biology, 24, 3010–3024, 2018.

Graham, H. V., Patzkowsky, M. E., Wing, S. L., Parker, G. G., Fogel, M. L., and Freeman, K. H.: Isotopic characteristics of canopies in simulated leaf assemblages, Geochimica et Cosmochimica Acta, 144, 82–95, 2014.

Greenop, R., Sosdian, S. M., Henehan, M. J., Wilson, P. A., Lear, C. H., and Foster, G. L.: Orbital forcing, ice volume, and CO_2 across the Oligocene–Miocene transition, Paleoceanography and Paleoclimatology, 34, 316–628, 2019.

Hansen, J., Sato, M., Russell, G., and Kharecha, P.: Climate sensitivity, sea level and atmospheric carbon dioxide, Philosophical Transactions of the Royal Society A, 371, 20120294, 2013.

Henrot, A.-J., François, L., Favre, E., Butzin, M., Ouberdous, M., and Munhoven, G.: Effects of CO_2, continental distribution, topography and vegetation changes on the climate at the Middle Miocene: a model study, Climate of the Past, 6, 675–694, 2010.

Herold, N., Müller, R. D., and Seton, M.: Comparing early to middle Miocene terrestrial climate simulations with geological data, Geosphere, 6, 952–961, 2010.

Ji, S., Nie, J., Lechler, A., Huntington, K. W., Heitmann, E. O., and Breecker, D. O.: A symmetrical CO_2 peak and asymmetrical climate change during the middle Miocene, Earth and Planetary Science Letters, 499, 134–144, 2018.

Kaulfuss, U.: Crater stratigraphy and the post-eruptive evolution of Foulden Maar, southern New Zealand, New Zealand Journal of Geology and Geophysics, 60, 410–432, 2017.

Kaulfuss, U., Lee, D. E., Barratt, B. I. P., Leschen, R. A. B., Larivière, M.-C., Dlussky, G. M., Henderson, I. M., and Harris, A. C.: A diverse fossil terrestrial arthropod fauna from New Zealand: evidence from the early Miocene Foulden Maar fossil lagerstätte, Lethaia, 48, 299–308, 2015.

Kohn, M.J.: Carbon isotope discrimination in C3 land plants is independent of natural variations in p_{CO2}, Geophysical Perspective Letters, 2, 35–43. 2016.

Kürschner, W. M.: The anatomical diversity of recent and fossil leaves of the durmast oak (*Quercus petraea* Lieblein/*Q. pseudocastanaea* Goeppert) — implications for their use as biosensors of palaeoatmospheric CO_2 levels, Review of Palaeobotany and Palynology, 96, 1–30, 1997.

Kürschner, W. M., Kvaček, Z., and Dilcher, D. L.: The impact of Miocene atmospheric carbon dioxide fluctuations on climate and the evolution of terrestrial ecosystems, PNAS, 105, 449–453, 2008.

Kürschner, W. M. and Kvaček, Z.: Oligocene-Miocene CO_2 fluctuations, climatic and palaeofloristic trends inferred from fossil plant assemblages in central Europe, Bulletin of Geosciences, 84, 189–202, 2009.

Leathwick, J. R.: New Zealand's potential forest pattern as predicted from current species-environment relationships, New Zealand Journal of Botany, 39, 447–464, 2001.

Lee, D. E., Lindqvist, J. K., Beu, A. G., Robinson, J. H., Ayress, M. A., Morgans, H. E. G., and Stein, J. K.: Geological setting and diverse fauna of a Late Oligocene rocky shore ecosystem, Cosy Dell, Southland, New Zealand Journal of Geology and Geophysics, 57, 195–208, 2014.

Lee, D. E., Kaulfuss, U., Conran, J. G., Bannister, J. M., and Lindqvist, J. K.: Biodiversity and palaeoecology of Foulden Maar: an early Miocene *Konservat-Lagerstätte* deposit in southern New Zealand, Alcheringa, 40, 525–541, 2016.

Liebrand, D., de Bakker, A. T. M., Beddow, H. M., Wilson, P. A., Bohaty, S. M., Ruessink, G., Pälike, H., Batenburg, S. J., Hilgen, F. J., Hodell, D. A., Huck, C. E., Kroon, D., Raffi, I., Saes, M. J. M., van Dijk, A. E., and Lourens, L. J.: Evolution of the early Antarctic ice ages, PNAS, 114, 3867–3872, 2017.

Lindqvist, J. K. and Lee, D. E.: High-frequency paleoclimate signals from Foulden Maar, Waipiata Volcanic Field, southern New Zealand: An Early Miocene varved lacustrine diatomite deposit, Sedimentary Geology, 222, 98–110, 2009.

Londoño, L., Royer, D. L., Jaramillo, C. A., Escobar, J., Foster, D. A., Cárdenas-Rozo, A. L., and Wood, A.: Early Miocene CO_2 estimates from a Neotropical fossil leaf assemblage exceed 400 ppm, American Journal of Botany, 105, 1929–1937, 2018.

Long, S. P., Ainsworth, E. A., Rogers, A. and Ort, D. R.: Rising atmospheric carbon dioxide: Plants FACE the future, Annual Review of Plant Biology, 55, 591–628, 2004.

Maire, V., Wright, I. J., Prentice, I. C., Batjes, N. H., Bhaskar, R., van Bodegom, P. M., Cornwell, W. K., Ellsworth, D. S., Niinemets, Ü., Ordonez, A., Reich, P. B., and Santiago, L. S.: Global effects of soil and climate on leaf photosynthetic traits and rates, Global Ecology and Biogeography, 24, 706–717, 2015.

Marrero, T. R. and Mason, E. A.: Gaseous diffusion coefficients, Journal of Physical and Chemical Reference Data, 1, 3–118, 1972.

McElwain, J. C., Montañez, I. P., White, J. D., Wilson, J. P., and Yiotis, C.: Was atmospheric CO_2 capped at 1000 ppm over the past 300 million years?, Palaeogeography, Palaeoclimatology, Palaeoecology, 441, 653–658, 2016.

Mejía, L. M., Méndez-Vicente, A., Abrevaya, L., Lawrence, K. T., Ladlow, C., Bolton, C., Cacho, I. and Stoll, H.: A diatom record of CO_2 decline since the late Miocene, Earth and Planetary Science Letters, 479, 18–33, 2017.

Moraweck, K., Grein, M., Konrad, W., Kvaček, J., Kovar-Eder, J., Neinhuis, C., Traiser, C., and Kunzmann, L.: Leaf traits of long-ranging Paleogeone species and their relationship with depositional facies, climate an atmospheric CO_2 level, Palaeontographica Abteilung B, 298, 93–172, 2019.

Németh, K. and White, J. D. L.: Reconstructing eruption processes of a Miocene monogenetic volcanic field from vent remnants: Waipiata Volcanic Field, South Island, New Zealand, Journal of Volcanology and Geothermal Research, 124, 1–21, 2003.

Niinemets, Ü., Díaz-Espejo, A., Flexas, J., Galmés, J., and Warren, C. R.: Role of mesophyll diffusion conductance in constraining potential photosynthetic productivity in the field, Journal of Experimental Botany, 60, 2249–2270, 2009.

655   Niinemets, Ü., Flexas, J., and Peñuelas, J.: Evergreens favored by higher responsiveness to increased
656   CO_2, TRENDS in Ecology and Evolution, 26, 136–142, 2011.

657   Norby, R. J., Sholtis, J. D., Gunderson, C. A. and Jawdy, S. S.: Leaf dynamics to a deciduous forest
658   canopy: no response to elevated CO_2, Oecologia, 136, 574–584, 2003.

659   Polissar, P. J., Rose, C., Uno, K. T., Phelps, S. R., and DeMenocal, P.: Synchronous rise of African C_4
660   ecosystems 10 million years ago in the absence of aridification, Nature Geoscience, 12, 657–660,
661   2016.

662   Reichgelt, T., Kennedy, E. M., Mildenhall, D. C., Conran, J. G., Greenwood, D. R., and Lee, D. E.:
663   Quantitative palaeoclimate estimates for Early Miocene southern New Zealand: Evidence from
664   Foulden Maar, Palaeogeography, Palaeoclimatology, Palaeoecology, 378, 36–44, 2013.

665   Reichgelt, T., D'Andrea, W. J., and Fox, B. R. S.: Abrupt plant physiological changes in southern New
666   Zealand at the termination of the Mi-1 event reflect shifts in hydroclimate and $p$$CO_2$, Earth and
667   Planetary Science Letters, 455, 115–124, 2016.

668   Reichgelt, T. and D'Andrea, W. J.: Plant carbon assimilation rates in atmospheric CO_2 reconstructions,
669   New Phytologist, 223, 1844–1855, 2019.

670   Reichgelt, T., Kennedy, E. M., Conran, J. G., Lee, W. G., and Lee, D. E.: The presence of moisture
671   deficits in Miocene New Zealand, Global and Planetary Change, 172, 268–277, 2019.

672   Retallack, G. J. and Conde, G. D.: Deep time perspective on rising atmospheric CO_2, Global and
673   Planetary Change, 189, 103177, 2020.

674   Roeske, C. A. and O'Leary, M. H.: Carbon isotope effects on the enzyme-catalyzed carboxylation of
675   ribulose bisphosphate, Biochemistry, 23, 6275–6284, 1984.

676   Royer, D. L.: Climate sensitivity in the geologic past, Annual Review of Earth and Planetary Sciences,
677   44, 277–293, 2016.

678   Royer, D. L., Moynihan, K. M., McKee, M. L., Londoño, L., and Franks, P. J.: Sensitivity of a leaf gas-
679   exchange model for estimating paleoatmospheric CO_2 concentration, Climate of the Past, 15, 795–809,
680   2019.

681   Rubel, F. and Kottek, M.: Observed and projected climate shifts 1901–2100 depicted by world maps of
682   the Köppen-Geiger climate classification, Meteorologische Zeitschrift, 19, 135–141, 2010.

683   Šantrůček, J., Vráblová, M., Šimková, M., Hronková, M., Drtinová, M., Květoň, J., Vrábl, D., Kubásek,
684   J., Macková, J., Wiesnerová, D., Neuwithová, J., and Schreiber, L.: Stomatal and pavement cell
685   density linked to leaf internal CO_2 concentration, Annals of Botany, 114, 191–202, 2014.

686   Schneider, C. A., Rasband, W. S., and Eliceiri, K. W.: NIH Image to ImageJ: 25 years of image analysis,
687   Nature Methods, 9, 671–675, 2012.

688   Schuepp, P. H.: Transley Review No. 59 Leaf boundary layers, New Phytologist, 125, 477–507, 1993.

689   Soh, W. K., Wright, I. J., Bacon, K. L., Lenz, T. I., Steinthorsdottir, M., Parnell, A. C., and McElwain, J.
690   C.: Palaeo leaf economics reveal a shift in ecosystem function associated with the end-Triassic mass
691   extinction event, Nature Plants, 3, 8, 2017.

692   Soh, W. K., Yiotis, C., Murray, M., Parnell, A. C., Wright, I. J., Spicer, R. A., Lawson, T., Caballero, R.,
693   and McElwain, J. C.: Rising CO_2 drives divergence in water use efficiency of evergreen and deciduous
694   plants, Science Advances, 5, eaax7906, 2019.

695   Spicer, R. A., Valdes, P. J., Spicer, T. E. V., Craggs, H. J., Srivastrava, G., Mehrotra, R. C., and Yang, J.:
696   New developments in CLAMP: Calibration using global gridded meteorological data,
697   Palaeogeography, Palaeoclimatology, Palaeoecology, 283, 91–98, 2009.

698   Steinthorsdottir, M., Vajda, V., and Pole, M. S.: Significant transient pCO$_2$ perturbation at the New
699   Zealand Oligocene–Miocene transition recorded by fossil plant stomata, Palaeogeography,
700   Palaeoclimatology, Palaeoecology, 515, 152–161, 2019.
701   Strömberg, C. A. E.: Evolution of grasses and grassland ecosystems, Annual Review of Earth and
702   Planetary Sciences, 39, 517–544, 2011.
703   Super, J. R., Thomas, E., Pagani, M., Huber, M., O'Brien, C., and Hull, P. M.: North Atlantic temperature
704   and pCO$_2$ coupling in the early-middle Miocene, Geology, 46, 519–522, 2018.
705   Tesfamichael, T., Jacobs, B. F., Tabor, N. J., Michel, L., Currano, E. D., Feseha, M., Barclay, R. S.,
706   Kappelman, J., and Schmitz, M.: Settling the issue of "decoupling" between atmospheric carbon
707   dioxide and global temperature: [CO$_2$]$_{atm}$ reconstructions across the warming Paleogene-Neogene
708   divide, Geology, 45, 999–1002, 2017.
709   Tipple, B. J., Meyers, S. R., and Pagani, M.: Carbon isotope of Cenozoic CO$_2$: A comparative evaluation
710   of available geochemical proxies, Paleoceanography, 25, PA3202, 2010.
711   Witkowski, C. R., Agostini, S., Harvey, B. P., van der Meer, M. T. J., Sinninghe Damsté, J. S., and
712   Schouten, S.: Validation of carbon isotope fractionation in algal lipids as a pCO$_2$ proxy using a natural
713   CO$_2$ seep (Shikine Island, Japan), Biogeosciences, 16, 4451–4461, 2019.
714   Yang, Y., Donohue, R. J., McVicar, T. R., Roderick, M. L. and Beck, H. E.: Long-term CO$_2$ fertilization
715   increases vegetation productivity and has little effect on hydrological partitioning in tropical
716   rainforests, Journal of Geophysical Research: Biogeosciences, 121, 2125–2140, 2016.
717   Zachos, J. C., Pagani, M., Sloan, L., Thomas, E., and Billups, K.: Trends, rhythms, and aberrations in
718   global climate 65 Ma to present, Science, 292, 686–693, 2001.
719   Zhou, S., Yu, B., Shwalm, C. R., Ciais, P., Zhang, Y., Fisher, J. B., Michalak, A. M., Wang, W., Poulter,
720   B., Huntzinger, D. N., Niu, S., Mao, J., Jain, A., Ricciuto, D. M., Shi, X., Ito, A., Wei, Y., Huang, Y.,
721   and Wang, G.: Response of water use efficiency to global environmental change based on output from
722   terrestrial biosphere models, Global Biogeochemical Cycles, 31, 1639–1655, 2017.
723   Zhu, Z., Piao, S., Myneni, R. B., Zeng, Z., Canadell, J. G., Ciais, P., Sitch, S., Friedlingstein, P., Arneth,
724   A., Cao, C., Cheng, L., Kato, E., Koven, C., Li, Y., Lian, X., Liu, Y., Liu, R., Mao, J., Pan, Y., Peng,
725   S., Peñuelas, J., Poulter, B., Pugh, T. A. M., Stocker, B. D., Viovy, N., Wang, X., Wang, Y., Xiao, Z.,
726   Yang, H., Zaehle, S., and Zeng, N.: Greening of the Earth and its drivers, Nature Climate Change, 6,
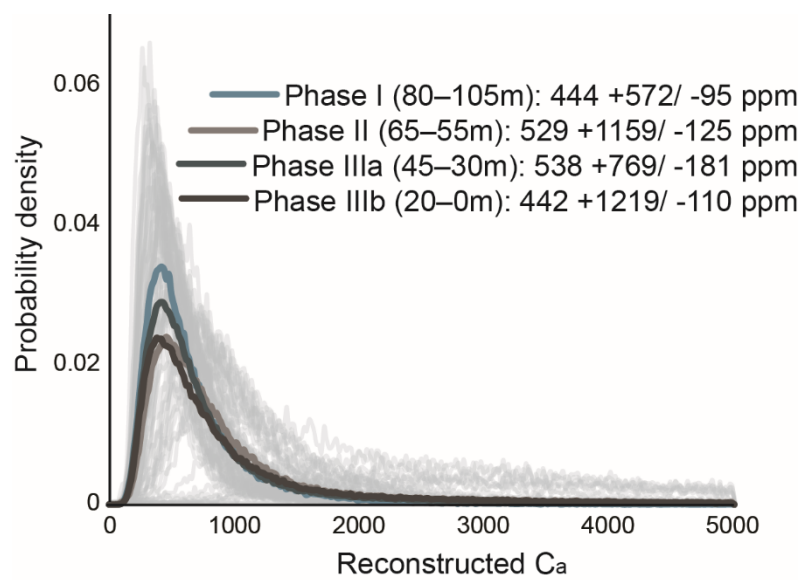727   791–795, 2016.
728
729

731

732
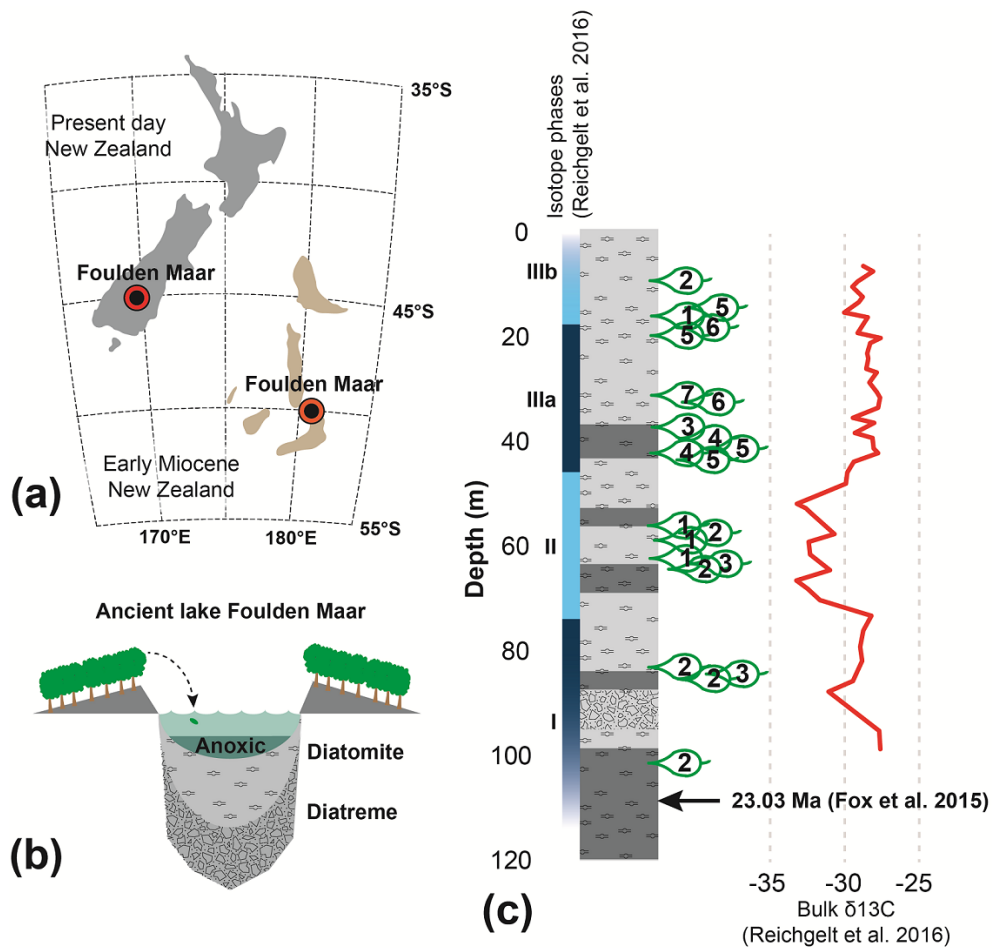
Figure 1. Foulden Maar site information. (a) Location of the Foulden Maar deposit and paleogeographic

reconstruction of early Miocene New Zealand (Boyden et al., 2011; Lee et al., 2014). (b) Schematic

reconstruction of the Foulden Maar depositional environment. (c) Stratigraphic column of the Foulden

Maar core (Fox et al., 2015), with sample locations and bulk organic δ^{13}C (Reichgelt et al., 2016).

737

738   Fig. 2
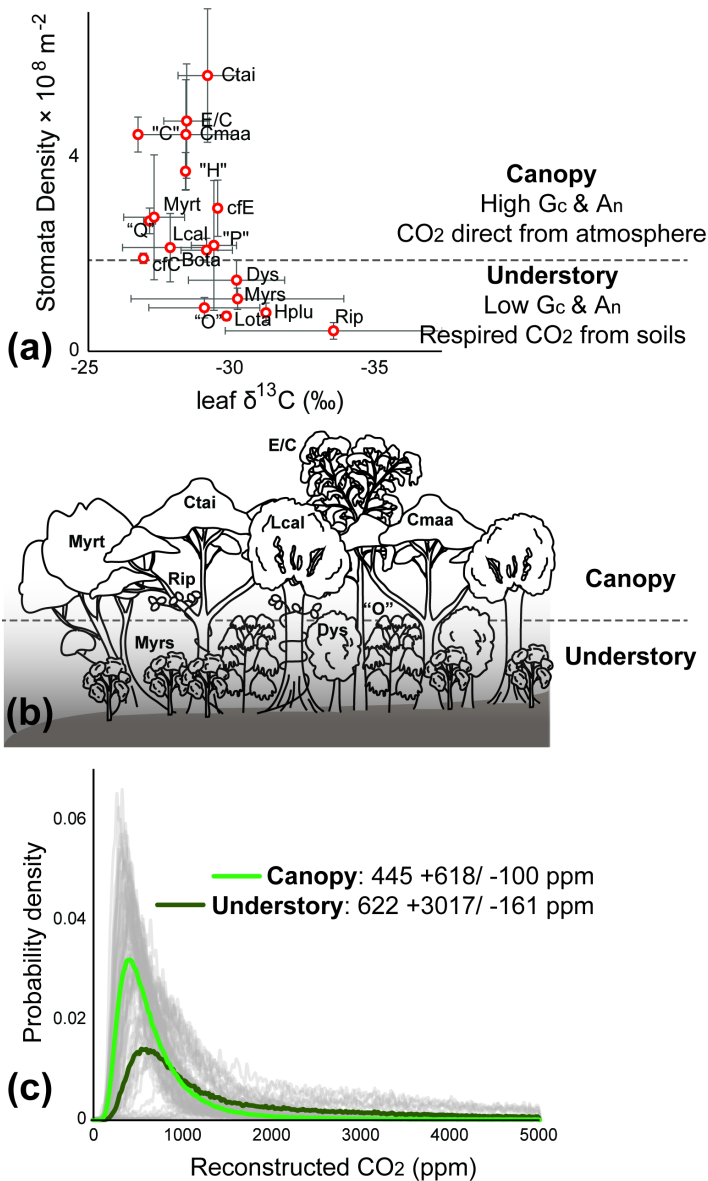
Figure 2. Foulden Maar paleoecology and atmospheric CO₂ reconstructions. (a) $\delta^{13}C$ values and stomatal density (error bars representing $\pm 1\sigma$) from the fossil leaves of Foulden Maar provide constraints to distinguish canopy leaf types from understory, because understory leaves tend to have a high range of $\delta^{13}C$ and low cell density (Graham et al., 2014; Bush et al., 2017). **(b)** Paleoecological reconstruction of the dense rainforest at Foulden Maar with a canopy comprising *Litsea calicarioides* (Lcal), *Cryptocarya taieriensis* (Ctai), *C. maarensis* (Cmaa), cf. Elaeocarpaceae/Cunoniaceae (E/C), and cf. Myrtaceae (Myrt), and an understory comprising cf. *Myrsine* (Myrs), cf. *Ripogonum* (Rip), cf. *Dysoxylum*

747 (Dys), and leaf type "O". *Hedycarya pluvisilva* (Hplu), *Laurelia otagoensis* (Lota), *Beilschmiedia*

748 *otagoensis* (Bota), cf. *Cryptocarya* (cfC), cf. *Endiandra* (cfE), and leaf types "C", "H", "P", and "Q"

749 could not be ecologically placed with certainty. **(c)** Probability density distributions of C_a reconstructions

750 from canopy (thick light green line) and understory components (thick dark green line) using a gas-

751 exchange model (Franks et al., 2014). Grey curves represents the probability distribution of 10,000

752 Monte Carlo reconstructions on a single fossil leaf.

753

754

Figure with y-axis "Probability density" (0 to 0.06) and x-axis "Reconstructed C_a" (0 to 5000). Legend:
- Phase I (80–105m): 444 +572/ -95 ppm
- Phase II (65–55m): 529 +1159/ -125 ppm
- Phase IIIa (45–30m): 538 +769/ -181 ppm
- Phase IIIb (20–0m): 442 +1219/ -110 ppm

755 **Figure 3.** Probability density distributions of Ca reconstructions using a gas-exchange model (Franks et

756 al., 2014), divided by bulk carbon isotope phases (Fig. 1c).

757

758 Fig. 4
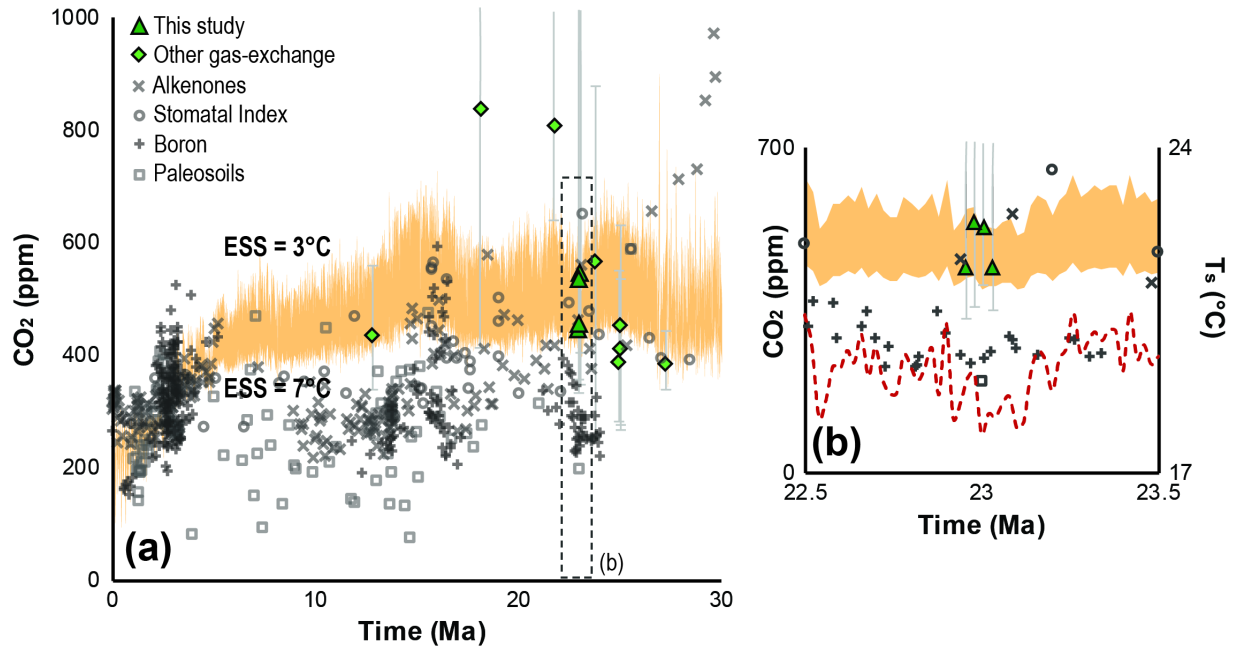
Figure 4. Neogene Earth System Sensitivity (ESS) and C_a reconstructions. Calculated C_a levels for an ESS range of 3–7 °C (orange shaded area) for the last 30 Ma **(a)**, and for the interval between 22.5–23.5 Ma **(b)**, the red dashed line in **(b)** indicates the global average surface temperature (T_s) in the earliest Miocene (Hansen et al., 2013). The ESS envelope was determined using deep-sea $\delta^{18}O$ of benthic foraminifera (Zachos et al., 2001) and the transform function approach from Hansen et al. (2013) (Supplementary Information). Proxy-based Neogene C_a reconstructions are derived from a previously published compilation (Foster et al., 2017) and are supplemented with more recently published data (Ji et al., 2019; Londoño et al., 2018; Super et al., 2018; Greenop et al., 2019; Moraweck et al., 2019, Steinthorsdottir et al., 2019). Error bars on gas-exchange based proxy estimates represent ±1σ.

Fig. 5
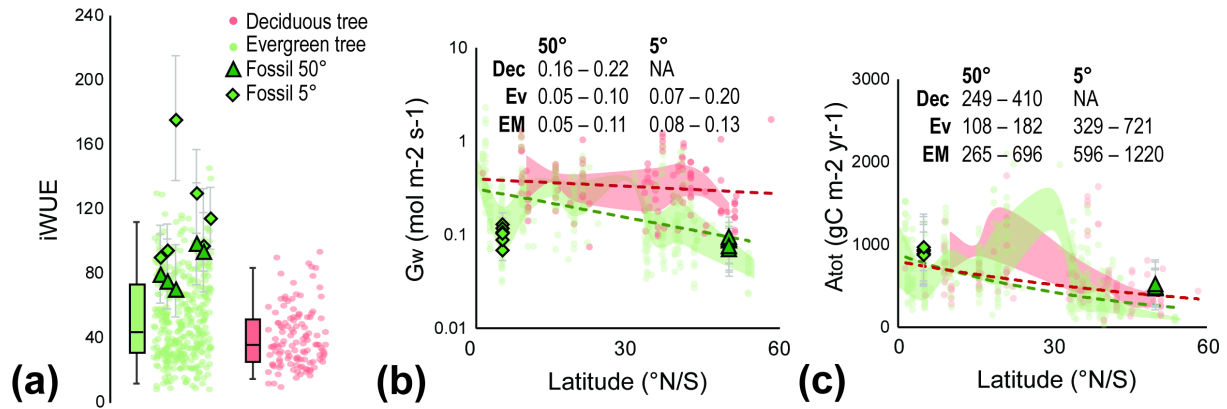
Figure 5. Early Miocene leaf-level physiological parameters of canopy trees. (a) Intrinsic water-use efficiency (iWUE) of evergreen (green circles) and deciduous trees (red circles) based on modern leaf-level measurements (Maire et al., 2015), and fossil reconstructions (green triangles and diamonds). Error bars on fossil-derived data indicate ±1σ, box-and-whisker plots indicate median, first and third quartile (Q1 and Q3), and 95% confidence interval of modern leaves of canopy trees. Individual datapoints are randomized on the x-axis for a clearer depiction of the distribution. **(b)** Conductance to water (G_w) from modern evergreen (Ev) and deciduous (Dec) trees (Maire et al., 2015) and fossils (EM) from different latitudes. The shaded red and green areas indicate the Q1–Q3 range of modern evergreen and deciduous trees, respectively, and the dashed lines indicate the overall linear trend with latitude. Text in panel is the Q1–Q3 range for each group, grouped in 5° latitude bins. **(c)** Total annual carbon flux per unit leaf area (A_{tot}) from modern evergreen (Ev) and deciduous (Dec) trees (Maire et al., 2015) and fossils (EM) from different latitudes. The shaded red and green areas indicate the Q1–Q3 range of modern evergreen and deciduous trees, respectively, and the dashed lines indicate the overall exponential trend with latitude. Text in panel is the Q1–Q3 range for each group, grouped in 5° latitude bins.

Data availability. All raw measurement data on fossil leaves generated for this paper is available in the online supplementary information. Raw measurements on fossil leaves from Ethiopia (Tesfamichael et al., 2017) and Panama (Londoño et al., 2018), $\delta^{18}O$ measurements (Zachos et al., 2001), and iWUE, G_w

790   and A_n measurements on modern plants (Maire et al., 2015) are available through the cited original

791   works.

792